# UNVEILING SALT TRANSPORT AND DAMAGE IN POROUS ROCK AT THE PORE-SCALE THROUGH 4D X-RAY IMAGING AND DEEP LEARNING ANALYSIS

**S. Ben Elhadj Hamida[1], P. Moonen[2] and H. Derluyn[3]***

## Abstract

In this contribution, we illustrate how 4D X-ray micro-tomography contributes to a better understanding of the coupled hydro-chemo-mechanical processes occurring during salt weathering in a natural building stone. We focus on a Savonnières limestone sample consisting of a hydrophobically treated layer and a hydrophilic layer. The sample, saturated with NaCl solution, underwent drying/humidification cycles while being imaged at 9.4 µm resolution. Digital volume correlation (DVC) reveals that crystallization in the hydrophobic region generates stress, leading to crack formation, while deliquescence induces partial crack closure due to matrix swelling and salt dissolution. Deep learning segmentation (U-Net) allows precise tracking of drying and wetting sequences in the hydrophilic region, and salt crystallization in the hydrophobic region, at the scale of the different pore classes present in this limestone, having a multimodal pore structure.

**Keywords**: Building stone, X-ray micro-tomography, pore-scale transport, salt crystallization, salt damage.

## 1. Introduction

Salt precipitation may yield degradation in many building materials, including natural building stones. Each time salts precipitate in the material's pore space, mechanical stresses accumulate, potentially leading to fracturing of the material matrix. Hereby, new pathways for fluid transfer are created while simultaneously decreasing the integrity of the material, paving the way for an intensification of the degradation process during successive precipitation-dissolution cycles. Laboratory experimental studies typically focus on the macroscopic behaviour of specimens the size of small building blocks. Fewer studies explore the complex interaction between transport phenomena, salt precipitation, crack initiation and propagation at the pore-scale of building stones. To unravel these interconnected processes, non-destructive X-ray micro-computed tomography has proven to be a very powerful technique (Derluyn, 2024). In a previous contribution to the STONE conference series (Derluyn *et al.,* 2016), we demonstrated the potential of the then recently developed laboratory dynamic X-ray scanning technique for studying salt weathering phenomena in stones. Since then, significant advancements have been made in the application of artificial intelligence tools for analysing X-ray images. In this paper, we show how advanced image analysis techniques can overcome the challenges posed by spatial resolution in a limestone with a multimodal pore size distribution, ranging from tens of nanometres to hundreds of micrometres, while also addressing contrast limitations in the X-ray images. With the establishment of X-ray facility networks, such as the EXCITE network (https://excite-network.eu/), which offer free access to X-ray scanners, we hope that conservators will take advantage of these advanced methodologies when deemed beneficial for addressing specific conservation challenges.

## 2. Materials and methods

### 2.1 Savonnières limestone and sodium chloride

Savonnières limestone has been used in the construction of historic monuments: in France, Savonnières has been used in the construction of many buildings, including the prefecture of Nancy, the Notre-Dame church, and the Saint-Dizier cathedral (Dessandier, 2000). Internationally, Savonnières stone has adorned significant buildings, including a museum in Amsterdam, the Netherlands, and the town hall of Leuven in Belgium (Denecker, 2015). Savonnières limestone is composed almost entirely of calcite, with a $CaCO_3$ concentration reaching 98% (Fronteau *et al.,* 2010). It is an oolitic stratified sedimentary rock, made up of spherical grains known as oolites. These oolites form around a nucleus and exhibit

[1] Syrine Ben Elhadj Hamida, Postdoctoral Researcher, Universite de Pau et des Pays de l'Adour, E2S UPPA, CNRS, LFCR, DMEX, Pau, France, syrine.ben-elhadj-hamida@univ-pau.fr

[2] P. Moonen, Professor, Universite de Pau et des Pays de l'Adour, E2S UPPA, CNRS, LFCR, DMEX, Pau, France, peter.moonen@univ-pau.fr

[3]* H. Derluyn, CNRS Associate Scientist, Universite de Pau et des Pays de l'Adour, E2S UPPA, CNRS, LFCR, DMEX, Pau, France, hannelore.derluyn@univ-pau.fr

*Corresponding author

a radial and concentric structure. The cement, filling the pores between the oolites, consists of spathic calcite crystals arranged radially around the grains. This arrangement leads to the creation of triangular-shaped pores. According to Roels *et al.,* 2003, this heterogeneous rock presents four types of porosity: (1) intergranular microporosity, (2) intergranular macroporosity, (3) intragranular microporosity and (4) intragranular macroporosity. Roels *et al.* (2003) found that Savonnière rock consists of five pore systems, with characteristic radius of 0.1 µm, 0.7 µm, 12 µm, and two systems of 87 µm. The first and second pore systems represent the intragranular microporosity of the oolites, the third system represents the intergranular micropores between the spathic calcite crystals, and the fourth and fifth systems correspond to macropores with a high level of porosity (Figure 1). Above 0°C, sodium chloride (NaCl) has a single stable solid phase: anhydrous halite. This phase begins to precipitate at concentrations around 6 molal, the solubility limit of NaCl in water, which is only slightly temperature dependent. Below this concentration, the salt remains fully dissolved. In addition, NaCl begins to deliquesce at around 75% relative humidity (RH). Deliquescence refers to the phase transition that occurs when a deliquescent solid, such as NaCl, absorbs water vapor from the atmosphere and dissolves to form an aqueous solution. This process begins at a specific relative humidity, known as the deliquescence point, above which the salt solution becomes thermodynamically stable (Martin, 2000); (Dupas-langlet, 2013). At this threshold, solid NaCl can coexist with its saturated solution, whereas above it, only the liquid phase remains.

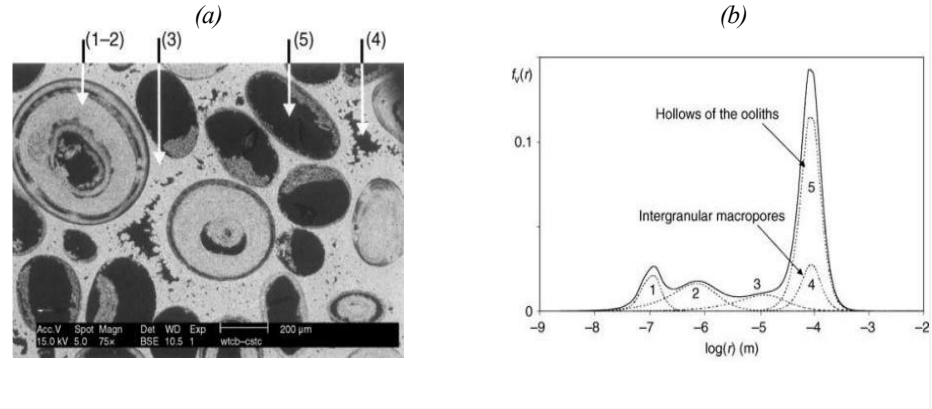


*Figure 1: (a) SEM-image and (b) pore volume distribution as a function of pore radius for Savonnières limestone (after (Roels et al., 2003)).*

## 2.2 Crystallization-deliquescence experiment

The considered experiment focuses on a cylindrical sample of Savonnières rock with a diameter of 8.4 mm and a height of 9 mm. A hydrophobic treatment SILRES® BS280 (Wacker) was applied to the upper surface of the sample in order to prevent efflorescence. To seal the sample on the lateral sides and prevent salt efflorescence on these surfaces as well as the loss of small rock debris, an aluminium tape was carefully wrapped around its circumference, while leaving the top and bottom surfaces exposed. The sample was subsequently put in contact with a 6 molal NaCl saline solution at its base. Capillary imbibition took place over a period of 1.5 hours after which the bottom surface was also covered with an aluminium tape. The capillary saturated sample was then placed in a cylindrical plastic cell connected to a humidity generator, and equipped with an RH-T sensor (SHT75) for independent climate monitoring. This cell was positioned inside the EMCT X-ray scanner (UGCT, Ghent, Belgium (Dierick *et al.,* 2014)) and time-lapse scanning was performed during drying-induced crystallization and deliquescence. Drying occurred at 5% RH and 26 °C with scans taken every 30 minutes over a period of 20 hours. After the sample was completely dried out, deliquescence was triggered by increasing RH to 93%, with scans acquired every hour for 23 hours. Each scan lasted 10 minutes. A total of 62 scans were acquired, with each scan (i.e., each reconstructed 3D volume), consisting of 1200 slices with a voxel size of 9.4 µm. To minimize cone-beam artefacts, the sample was positioned so that the upper third section of the projection images consisted of air, resulting in a coverage of 80% of the sample's height within the field of view.

## 2.3 Image processing

### *2.3.1 Raw data*

The image processing workflow is defined after careful inspection of the raw data. Initially, we analyse a single 2D slice through time and focus on the events taking place within the different porosity classes. The visual examination of raw images during the experiment (Figure 2) allows for the identification of certain macropores, mainly intergranular, filled with saline solution in the initial saturated state of the sample, as illustrated in image 1a. These pores empty during the drying process (image 1b). At the end of the deliquescence, these pores refill, either completely or partially, in comparison to their initial state (images 1c). Visual observations also revealed that the hydrophobic upper part of the sample suffered

damage, with the appearance of cracks, as shown in cross-section 2b at the end of the drying. Examination of other images reveals that these cracks are small in size and have a non-uniform distribution. At the end of deliquescence, some of these cracks tend to close, either partially or completely, as illustrated in image 2c.

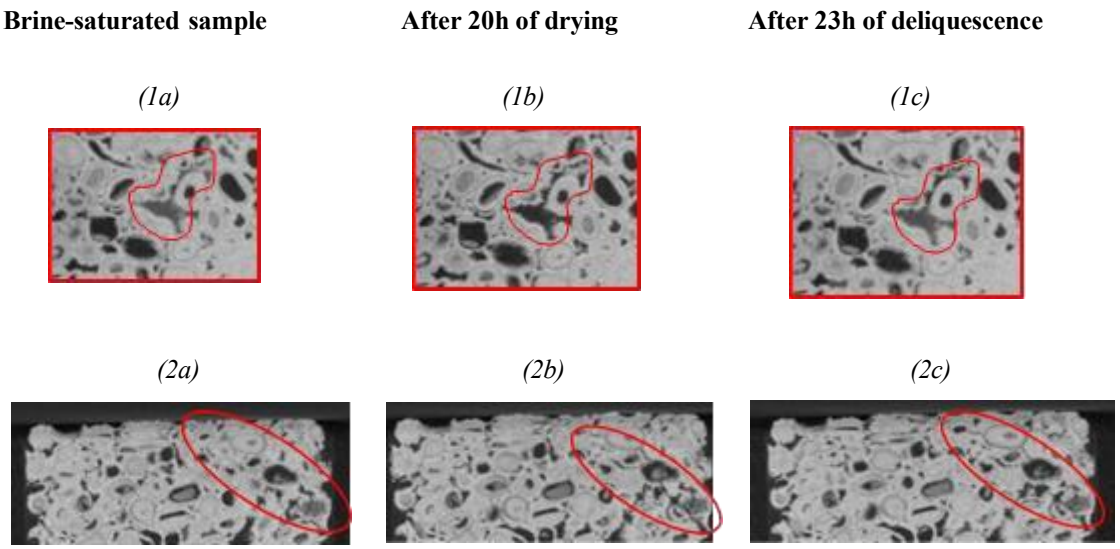


*Figure 2: Qualitative identification of different effects on the rock from raw data.*

The greyscale distribution of the capillary-saturated rock sample reveals two dominant intensity ranges: one corresponding to air (darker grey levels) and another to the rock matrix (brighter grey levels). Between these two, an overlapping zone exists which could include both the saline solution or represent portions of the matrix with a different amount of (unresolved) porosity, particularly the interior of ooids. This ambiguity results from partial volume effects, where multiple phases coexist within a single voxel, making it difficult to accurately discriminate between individual phases based solely on greyscale intensity.

### *2.3.2 Digital volume correlation*

To account for the internal deformation within the sample, we applied Digital Volume Correlation (DVC) using the SPAM toolkit (Stamati *et al.,* 2020). DVC identifies the transformation between two 3D images of the same sample: a reference image (noted as im1) and a later image (noted as im2) showing deformation. This technique was applied to both drying and deliquescence processes. For drying, the first image (sample saturated with saline solution) serves as the reference, and subsequent scans acquired every 30 minutes are compared. For deliquescence, the reference is the first scan after 1 hour at high humidity, with comparisons made every hour. The DVC workflow starts with a multiscale registration, aligning the two volumes, and providing a global estimation of deformation. Subsequently, local digital image correlation (LDIC) refines the deformation field by performing local, non-rigid correlations on a structured grid of sub-volumes. The calculated deformation is then applied to the reference image (im1def), and its subtraction from the target image (im2) yields a residual field (im2 – im1def). This highlights localized changes (e.g., salt formation or dissolution) not visible in raw images or simple subtractions. It enables quantification of salt, monitoring of drying/deliquescence kinetics, and visualization of transport in unresolved pores. Finally, the strain field is derived from the displacement field obtained by LDIC. Among the available methods, the Q8 finite element method provided optimal results for our dataset.

### *2.3.3 Pore scale analysis with deep learning*

As described in Section 2.1, Savonnières limestone contains four types of porosity: two macropore types (resolved in the scans) and two micropore types (unresolved). Intergranular macropores are located between calcite cements, while intragranular macropores are found inside partially or fully hollow ooids. The micropores, which appear as part of the matrix due to their sub-resolution size, are either intragranular (within ooid cores) or intergranular (between cement crystals). As these pore families have similar X-ray absorption, traditional segmentation methods based on greyscale contrast were ineffective. Therefore, we used deep learning-based segmentation with a U-Net model, defining cement within ooids as intragranular micropores, and cement between grains as intergranular micropores. The segmentation was performed using Dragonfly software (Dragonfly 2022), following a structured workflow. From a 3D image of the Savonnières stone (1076 slices), 10 slices were manually labelled to identify four pore families: intragranular macropores, intergranular macropores, intragranular micropores, and intergranular micropores. Data augmentation techniques were then applied, resulting in a training dataset of 1010 images. Once trained, the U-Net model was applied to track the

evolution of each pore family during drying and deliquescence. To do so, deformation fields were computed using the DVC workflow between each scan and a reference image (the initial scan of the saturated sample). The reference image was deformed accordingly and segmented with the trained U-Net. For example, the reference scan 'sav01' was deformed relative to scan 'sav02' (after 30 minutes of drying) to produce 'sav01deformed%sav02', which was then segmented. This process was repeated across all time steps for both drying and deliquescence. From each segmented, deformed reference image, masks corresponding to each pore family were extracted and applied to the respective difference images (residual field). For instance, the masks from 'sav01deformed%sav02' were applied to 'sav02–sav01deformed%sav02'. Finally, the average grey level for each pore family was calculated along each slice over the full height of the sample in 3D. This approach ensures accurate alignment between pore family masks and difference images across all time steps, enabling a consistent temporal analysis of salt dynamics in each pore type.

## 3. Results

### 3.1 Hydrophobic zone

In the hydrophobic part, complex physical interactions are observed, including mechanical behaviour characterized by crack formation and closure, associated with salt accumulation. These observations are supported by the calculation of volumetric strain using the DVC workflow. The distribution of volumetric strain across the sample height shows small negative volumetric strains at the onset of drying, caused by a slight shrinkage due to evaporation. Over time, volumetric strain becomes positive in this region, primarily due to salt crystallization, leading to local material expansion (Figure 3). This expansion is not homogeneous, resulting in heterogeneous internal stresses. These deformations may arise from various factors, such as shear forces from salt crystals, heterogeneities in the rock, or variations in mechanical properties. When cumulative volumetric strain exceeds the rock's mechanical resistance, cracks can form. These cracks coincide spatially with regions of high volumetric deformation, as seen in the 2D strain field representations.

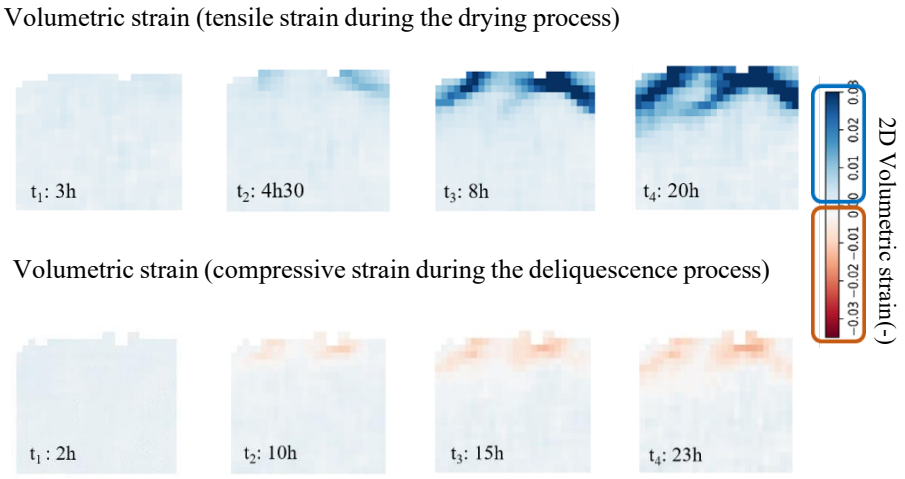


*Figure 3: 2D fields of volumetric strain along the height of the sample during the drying process and the deliquescence process (after Ben Elhadj Hamida, 2024).*

The first stage of the deliquescence process is characterized by positive volumetric strains (Figure 3), indicating swelling due to moisture absorption. This is attributed to the hygroscopic behaviour of NaCl, which absorbs moisture at around 75% relative humidity. As pores expand, local swelling occurs. Subsequently, negative volumetric strain indicates salt dissolution, reducing the volume of salt crystals and causing pore shrinkage. 2D fields of volumetric strain show that cracks formed during drying start to close as negative volumetric strain increases. This closure may result from several phenomena linked to the high humidity: swelling of the matrix, generating radial forces that push crack walls together (especially for thin cracks), and dissolution of NaCl, reducing crystal volume that allows to reduce crack openings.

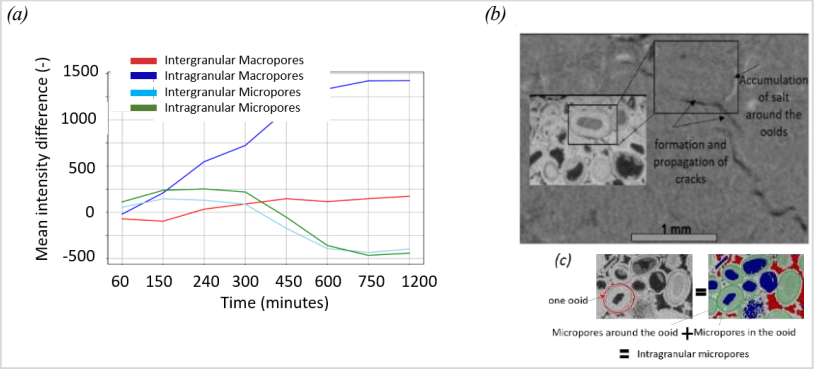


*Figure 4: (a) Temporal evolution of the average greyscale level differences, derived from difference images, during the drying process in the hydrophobic region of the sample for each pore family, (b) cross section showing the final state of the sample at the end of drying with the appearance of fissures, (c) different micropores in an around the ooids and macropores (colour-coded as in Figure 4 (a)), identified with deep-learning segmentation (after Ben Elhadj Hamida 2024).*

The variation in average grey level for different pore families during drying (Figure 4a & 4c) shows that intragranular macropores exhibit the strongest increase, indicating significant salt formation in these zones compared to intergranular macropores. A moderate increase is also observed in intragranular and intergranular micropores, consistent with their relatively smaller size. The greater salt accumulation in intragranular macropores may result from the non-uniform fluid transport in the hydrophobic zone.

During imbibition, the intergranular macropores, more exposed to the exterior, might have been preferentially affected by the hydrophobic treatment, leaving the intragranular macropores more accessible to the saline solution. This behaviour is visually confirmed by the difference images showing predominant salt deposition in intragranular macropores. Regarding the increase in salt within intragranular micropores, particularly around the ooids, the difference images reveal salt deposition around these structures (Figure 4b). A subsequent decrease in grey level in the micropores corresponds to crack formation.

More fissures are observed in intergranular micropores than in intragranular ones. This suggests that fractures initiate in areas of significant salt accumulation around ooids, where mechanical fragility is highest. Consequently, ooids are subjected to two sources of salt-induced pressure: one from macropore crystallization and another from crystals in the surrounding microporosity. Cracks thus begin in these zones and propagate towards the surrounding calcite (segmented as intergranular micropores).

## 3.2 Hydrophilic zone

The hydrophilic part of the sample exhibits no notable damage or significant salt accumulation, which enables a more focused analysis of the transport kinetics in the Savonnières rock. From the 3D difference images obtained via the DVC workflow, the mean greyscale levels were calculated over the sample height (Figure 5a). During drying, curves trend uniformly towards negative values, showing progressive pore emptying. The drying rate is initially constant but slows down towards the end. Volumetric strain (Figure 3) shows a combination of small negative and positive values. Persistent negative values indicate shrinkage due to ongoing drying. Positive deformation values, appearing towards the end, reflect minor salt crystallization in small pores. The combination of segmentation using the U-Net model and difference image analysis from the DVC workflow provides a detailed picture of solution distribution in each pore family (Figure 5b). During drying, all pore families show a decrease in average grey level, indicating drying. Intergranular macropores, due to their larger size and exposure, begin drying first, as seen from their lower initial intensity values. The drying order follows the pore size: intergranular macropores, intragranular macropores, intergranular micropores, and finally intragranular micropores. Macropores dry rapidly then stabilize, whereas micropores show a delayed drying that accelerates over time. Difference images reveal that intergranular macropores are more often filled with saline solution than intragranular macropores. This explains the observed differences in their respective drying curves.

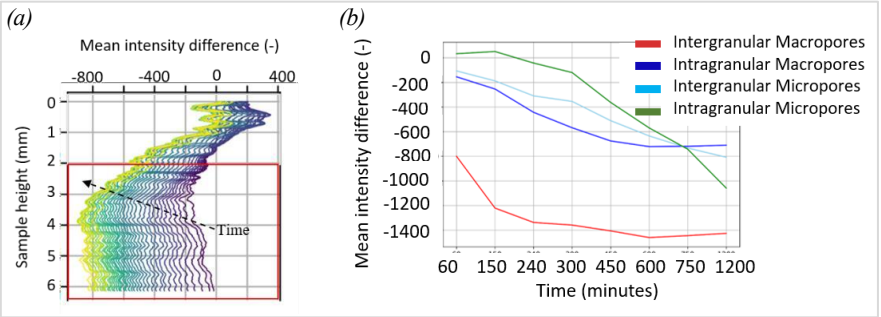


*Figure 5: (a) Drying profiles for the whole duration of the process in the hydrophilic part, (b) Evolution of the average grey level difference from difference images during drying in the hydrophilic part of the sample for each pore family (after Ben Elhadj Hamida 2024).*

The deliquescence phase unfolds in three stages characterized by a slow onset, a second acceleration stage, and eventual slowdown. Initially, precipitated salt deliquesces; then, dry pores facilitate absorption. As saturation increases, the absorption rate declines (Figure 6a). Volumetric strain (Figure 3) shows sustained positive values, confirming continuous swelling due to saline solution absorption. This aligns with the hydrophilic nature of this part of the rock. Simultaneously, small negative volumetric strain values suggest dissolution of residual salt crystals formed during drying. Their dissolution leads to minor pore shrinkage, a subtle effect that is however consistent with the expected reduction in crystal volume. The pore-filling sequence during deliquescence (Figure 6b) is the inverse of drying: intragranular micropores fill first, followed by intergranular micropores, intragranular macropores, and lastly intergranular macropores. When micropore grey level intensities begin stabilizing, macropores start filling, confirming a link between macro and micropore behaviour. Notably, intergranular macropores appear to absorb more saline solution than other pore types, corroborating their state observed at the beginning of drying (see also Figure 2).

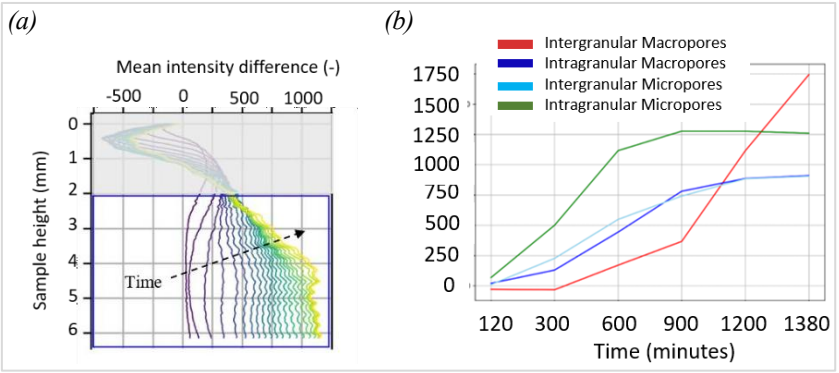


*Figure 6: (a) Deliquescence profiles for the whole duration of the process in the hydrophilic part, (b) Evolution of the average grey level difference from difference images during deliquescence in the hydrophilic part for each pore family (after Ben Elhadj Hamida 2024).*

## 4. Conclusions

We have shown that combining experimental observations with advanced imaging techniques and segmentation methods allows to reveal the interconnected phenomena related to salt crystallization and damage at the pore scale. The challenge now lies in applying these results in practice, for example, to increase the durability of building materials, or for the conservation of cultural heritage. Our study shows that we are capable of pinpointing the most vulnerable pore class for salt damage in a stone with a multimodal pore structure. To protect the stone from future damage, it is essential to ensure that treatments, such as crystallization inhibitors or consolidants, effectively penetrate this specific pore class.

## Acknowledgements

The authors acknowledge the financial support from the ERC Starting Grant PRD-Trigger (grant agreement No 850853).

## References

Ben Elhadj Hamida, S., 2024, Advanced image processing of dynamic X-ray tomography data to study salt crystallization and damage processes in Savonnières rock, PhD thesis, Université de Pau et des Pays de l'Adour, France.

Denecker, M., 2015, Le rôle des sulfates de sodium dans l'altération des pierres du patrimoine bâti: méthodes indirectes d'identification pour l'approche expérimentale, Ph.D. thesis, Université de Cergy-Pontoise, France.

Derluyn, H. 2024. Experimental observations on salt crystallization in geomaterials, in: Salt crystallization in porous media, H. Derluyn and M. Prat (eds.), ISTE-Wiley, ISBN: 978-1-78945-114-6, pp. 99-125.

Derluyn, H., Boone, M.A., Desarnaud, J., *et al.,* 2016, Quantifying salt crystallization dynamics in sandstone using 4D laboratory X-ray micro-CT, in Proceedings of the 13th International Congress on the Deterioration and Conservation of Stone, J.J. Hughes and T. Howind (eds.), Paisley, UK, pp. 83-90 (ISBN: 978-1-903978-57-3).

Dessandier, D., 2000, Guide méthodologique de sélection des pierres des monuments en termes de durabilité et compatibilité, Report BRGM/RP-50137-FR, Bureau de Recherches Géologiques et Minières, Orléans, France.

Dierick, M., Van Loo, D., Masschaele, B., Van den Bulcke, J., *et al.,* 2014, Recent Micro-CT Scanner Developments at UGCT, Nuclear Instruments and Methods in Physics Research Section B: Beam Interactions with Materials and Atoms, 324, 35–40.

Dupas-Langlet, M., 2013, De la déliquescence au mottage des poudres cristallines : cas du chlorure de sodium, Ph.D. thesis, Université de Technologie de Compiègne, France.

Fronteau, G., Moreau, C., Thomachot-Schneider, C., and Barbin, V., 2010, Variability of some Lutetian building stones from the Paris Basin, from characterisation to conservation, Engineering Geology, 115(3–4), 158–166.

Martin, S.T., 2000, Phase transitions of aqueous atmospheric particles, Chemical Reviews, 100(9), 3403–3453.

Roels, S., Carmeliet, J., and Hens, H., 2003, Modelling unsaturated moisture transport in heterogeneous limestone (Part 1. A mesoscopic approach), Transport in Porous Media, 52(1), 333–350.

Stamati, O., Andò, E., Roubin, E., *et al.,* 2020, SPAM: software for practical analysis of materials, Journal of Open-Source Software, 5(51), p. 2286.